



Fast, furious, and gassy: Etna's explosive eruption from the mantle

Anna Barth^{a,*}, Maxim Portnyagin^b, Nikita Mironov^c, Francois Holtz^d, Yves Moussallam^e, Estelle F. Rose-Koga^f, Daniel Rasmussen^g, Henry Towbin^h, Helge Gonnermannⁱ, Euan J. F. Mutch^{e,j,m}, Silvio G. Rotolo^{k,l}, Terry Plank^e

^a UC Berkeley Miller Institute, United States

^b GEOMAR Helmholtz Centre for Ocean Research Kiel, Germany

^c Vernadsky Institute of Geochemistry and Analytical Chemistry RAS, Russia

^d Institut für Mineralogie, Leibniz Universität Hannover, Germany

^e Lamont-Doherty Earth Observatory, United States

^f Institut des Sciences de la Terre d'Orléans, France

^g Peregrine Advisors, United States

^h Geological Institute of America, New York, United States

ⁱ Rice University, United States

^j Earth Observatory of Singapore, Nanyang Technological University, Singapore

^k Dipartimento di Scienze della Terra e del Mare, Università di Palermo, Italy

^l Istituto Nazionale di Geofisica e Vulcanologia, Sezione di Palermo, Italy

^m Asian School of the Environment, Nanyang Technological University, Singapore

ARTICLE INFO

Editor: Dr C. M. Petrone

Keywords:

Explosive eruption
Magma decompression rate
Melt inclusions
Volatiles
Carbonate
Etna

ABSTRACT

The 3930 BP Fall Stratified (FS) eruption at Mt. Etna is a rare example of a highly explosive eruption of primitive (picritic) magma directly from the mantle. The eruption produced ash plumes up to an estimated 20 km height, leading to a volcanic explosivity index (VEI) 4 (subplinian). Given its volatile-rich and primitive nature, the FS magma may have ascended rapidly from great depths to avoid fractionation and mixing within the extensive plumbing system beneath Etna. To determine the pressures from which the FS magma derived, we perform rehomogenization experiments on melt inclusions hosted in Fo₉₀₋₉₁ olivines to resorb shrinkage bubbles and determine the initial H₂O and CO₂ in the melt. With measured CO₂ concentrations of up to 9600 ppm, volatile solubility models yield magma storage pressures of 630–800 MPa. These correspond to depths of 24–30 km, which are comparable to the seismologically estimated Moho. Therefore, the magma's high CO₂ concentration must come from carbon in the mantle (likely from subducted carbonates), as opposed to assimilation of shallow (<10 km) crustal carbonates.

Diffusion modeling of H₂O and forsterite zonation profiles in clear, euhedral, and crystallographically oriented olivines indicates rapid ascent of magma directly from its source region to the surface. Forsterite profiles exhibit a narrow rim of growth zoning but no detectable diffusional zoning, reflecting maximum ascent times of 1–5 days. Eighteen measured H₂O profiles result in remarkably uniform decompression rates of 0.47 MPa/s (95% confidence interval of 0.16–1.28 MPa/s), which is among the fastest measured for basaltic-intermediate magmas. These decompression rates indicate that the final stage of magma ascent over the region in which H₂O degasses (between the surface and ~ 15 km) occurred extremely fast at ~ 17.5 m/s. This eruption may provide a link between primary magma composition and eruption intensity: we propose that the unusually explosive nature of this picritic eruption was driven by high H₂O and CO₂ concentrations, which led to continuously rapid ascent without stalling, all the way from the Moho.

* Corresponding author.

E-mail address: barthac@gmail.com (A. Barth).

<https://doi.org/10.1016/j.epsl.2024.118864>

Received 30 January 2024; Received in revised form 28 May 2024; Accepted 22 June 2024

Available online 19 July 2024

0012-821X/© 2024 Published by Elsevier B.V.

1. Introduction

Basaltic volcanism occurs over a vast range of scales and styles, from effusive lava flows, to Strombolian, Hawaiian, and up to Plinian eruption styles (e.g. Houghton and Gonnermann, 2008). Etna is a prime example of a volcano which hosts all of these eruption styles (Branca and Del Carlo, 2005; Coltelli et al., 1998; Zuccarello et al., 2022). The controls on eruption intensity remains poorly understood, especially for subplinian and plinian eruptions (Houghton and Gonnermann, 2008; Parfitt and Wilson, 1994). Subplinian and plinian eruptions are more typical for silicic magmas, where the explosive nature of the eruption is thought to be associated with brittle magma fragmentation. The latter is unlikely to occur in basaltic magmas because of their low viscosity (e.g. Giordano and Dingwell 2003, Houghton and Gonnermann 2008), yet several volcanoes are known to have hosted plinian eruptions of basaltic magma (Sunset craters – Allison et al. (2021), Masaya – Bamber et al. (2020), Etna – Coltelli et al. (1998), Tarawera – Houghton et al. (2004), Kīlauea – McPhie et al. (1990)).

In this context, the 3930 BP subplinian Fall Stratified (FS) eruption of picritic magma at Etna represents an extreme example of this mystery. The magma's high temperatures and H₂O concentration, and low SiO₂ concentrations and crystallinity, all act to lower viscosity (Coltelli et al., 2005; Kamenetsky et al., 2007), and yet this eruption was one of Etna's most explosive. The mystery of how to explosively erupt a low viscosity picritic magma is highlighted by their rarity; Coltelli et al. (2005) point out that the FS eruption is the only known subplinian eruption of picritic magma.

The uniformly primitive population of olivines within the FS magma (Fo 90–91) requires relatively fast magma ascent from at or near the Moho to avoid reequilibration toward lower forsterite compositions (e.g. Ruprecht and Plank 2013). Furthermore, the high density of picritic basalt makes it difficult to ascend through the entire span of the crust (Anderson, 1995), and requires that the vapor phase remains coupled with the melt in order to avoid stalling in the mid crust (Corsaro and Pompilio, 2004).

It has been proposed on the basis of experiments, modeling, and field observations of geysers, that the plume height (and explosivity) of an eruption is positively correlated with its source depth (Namiki and Manga, 2006; Reed et al., 2021). Shock tube experiments on bubble-bearing viscoelastic fluids show that more violent fragmentation occurs for larger pressure drops and initial bubble volume fractions (Namiki and Manga, 2006). Greater source depths and higher vesicularity mean more potential energy to be converted into kinetic energy and consequently faster decompression.

Coltelli et al. (2005) propose that the FS eruption was propelled by high volatile concentrations (in particular CO₂) causing early exsolution deep in the crust and consequently high rates of magma decompression. We aim to test this hypothesis by determining the primary volatile concentrations and decompression rates of the magma. Ultimately, we want to understand how a picritic magma is able to ascend through the entire crust without stalling, mixing with other magmas, or crucially, losing its vapor, in order to erupt with the most explosive intensity ever documented for a picritic magma.

1.1. Background

The Fall Stratified eruption of Etna (3930 BP) produced voluminous pyroclastic flow deposits (0.055 km³ dense rock equivalent – Coltelli et al., 2005), which attained thicknesses of 110 cm at distances of 7 km from the vent. The plume height has been estimated as 18–20 km from isopleth mapping corresponding to estimated mass eruption rates of 3.4–5.2 × 10⁷ kg/s and a high explosive energy (VEI 4, subplinian – Coltelli et al., 2005). As suggested by its name, the Fall Stratified eruption deposit consists of fine scale layering between finer and coarser lapilli. Coltelli et al. (2005) argue that the deposit reflects “the formation of a

sustained eruptive column” and interpret the layering to reflect oscillations in plume height and the lack of lithics and fine particles to support a magmatic rather than phreatic origin of the eruption. The FS eruption marks an important event in Etna's history – the productivity of explosive eruptions doubled after the FS eruption (Coltelli et al., 2000) (Fig. 1b), suggesting that it may have fundamentally altered the magmatic plumbing system beneath Etna and/or signaled a change in the mantle melting process (Fig. 1a). This is supported by the FS magma's anomalously high Rb/Nb ratios, which is typically high in subducting slab fluids/melts and thus thought to signify high input from subducted material (Fig. 1a).

Previous work has established key compositional features of the FS magma (Correale et al., 2014; Corsaro and Métrich, 2016; Gennaro et al., 2019; Kamenetsky et al., 2007). The magma is notable for its picritic composition – unusual for Mt. Etna and not erupted since the FS eruption. Whole rocks have 12–17 wt% MgO, melt inclusions (MIs) have 9–10 wt.% MgO, and most olivines are Fo 89–91. Note that Coltelli et al. (2005) find Fo as low as 83 but values <88 are restricted to microlites, extreme rims, or cores in rarely occurring reverse zoned crystals. Other studies (Kamenetsky et al., 2007; Gennaro et al., 2019) find exclusively Fo 89–91 olivines. Most olivines are unzoned (Coltelli et al., 2005). Another unusual aspect of the FS whole rocks and MIs is the high CaO/Al₂O₃ ratios (1.1–1.5; Kamenetsky et al., 2007), higher than any other eruptions at Etna and any subduction-adjacent magma in the world (e.g. Turner and Langmuir 2015). The tephra contains high Mg olivines, clinopyroxenes (Mg# 90–91), and Cr spinel. Inclusions of high Mg # clinopyroxenes within olivines indicate early crystallization – a sign of high pressures of crystallization (Kamenetsky et al., 2007) and also consistent with the high CaO/Al₂O₃. Furthermore, high volatiles concentrations (~ 4 wt% H₂O, 3500 ppm CO₂) have been measured in MIs, giving equilibrium pressures of ~ 500 MPa (Gennaro et al., 2019; Kamenetsky et al., 2007).

A major issue with the FS samples is that MIs contain a vapor bubble that is typically coated in Ca-Mg carbonates (Kamenetsky et al., 2007). Therefore, despite the already high measured CO₂ concentrations in the MIs' glass phase, true CO₂ concentrations and inferred equilibrium pressures are likely to be even higher. Previous work over the past years

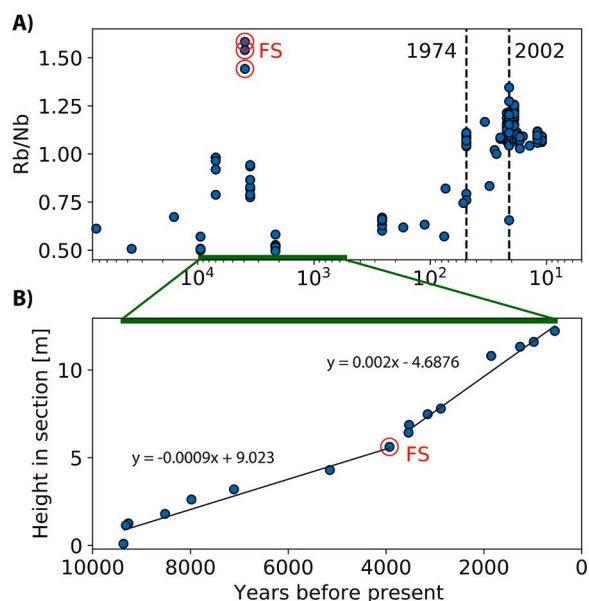


Fig. 1. a) Rb/Nb ratios over time highlighting uniqueness of FS eruption. Note the log scale of time, in order to show data from recent eruptions clearly. b) Height and age of Etna eruption deposits in stratigraphic section showing doubling of bulk sedimentation rate after the Fall Stratified Eruption. Also note hiatus of large eruptions for the ~1000 years prior to FS. Data and references listed in supplementary data table.

has demonstrated that the CO₂ concentrations in MI bubbles may contain > 80% of the bulk melt CO₂ (e.g. Moore et al. 2015), and so it is of paramount importance to reconstitute the CO₂ in MIs before being able to estimate both the depth of MI entrapment and the primary volatile contents of the magma.

2. Sample description

Tephra from the FS eruption was collected by Silvio Rotolo at the Torrente Fontanelle (see IGSN:10.58052/IEACB000Y for further details), and is the same sample as studied by Correale et al. (2014) and Gennaro et al. (2019). The tephra contains large (up to 5 mm) and euhedral olivine and clinopyroxene crystals, along with microcrystals of Cr-spinel (Coltelli et al., 2005; Gennaro et al., 2019; Kamenetsky et al., 2007). Olivine-hosted MIs show clear faceting with scalloped edges (Fig. 2). When viewed down the **b** axis MIs are typically oval to spherical, while along **a** or **c** they show a hexagonal shape. The ‘tips’ of the hexagons correspond to a plane (010) with a halo of micro fluid inclusions (present around all MIs, Fig. 2b). This texture has been described elsewhere and may indicate partial decrepitation (Anderson, 1974; Portnyagin et al., 2005). Cr-spinels are common inclusions in olivine, and occur in more than 70% of the studied MIs (Fig. 2, supplementary data table). Clinopyroxene can also be seen as inclusions within olivine (Fig. 2c) and were measured to have high Mg # (~90) by Kamenetsky et al. (2007).

All MIs contain a vapor bubble accounting for 3–10 vol% of the MI volume (Supplementary data table). There are no anomalously large bubbles, and bubble volume fraction correlates with MI size, typical of shrinkage bubbles and not those that are co-entrapped (Steele-MacInnis et al., 2017). The bubbles are typically coated in Ca-Mg-bearing carbonates (Fig. 2b and Kamenetsky et al., 2007). Many olivines contain

clearly decrepitated MIs, characterized by an abnormally large vapor bubble and patterns of fluid inclusions radiating from the MI along planar cracks (Fig. 2a) – these were avoided for further study. For modeling H^+ and Fo profiles within the olivine, we selected inclusion-free, euhedral olivines. Crystal orientation was determined from morphology and confirmed for 28 crystals with electron backscatter diffraction.

3. Methods

We used a suite of analytical and experimental methods. Novel techniques are highlighted here, while routine methods are detailed in the supplement.

3.1. Rehomogenization experiments

In order to redissolve the shrinkage bubble and associated carbonate back into the melt, we attempted to rehomogenize the MIs using a piston-cylinder, as in Rasmussen et al. (2020). These attempts were unsuccessful, likely because the quench rate was not fast enough (supplement). We had better success using a vertically oriented internally heated pressure vessel (IHPV) at the Institute of Mineralogy, Leibniz University in Hannover, which has faster quench rates and proved an effective tool for high-pressure rehomogenization experiments with MIs (e.g. Mironov et al. 2015). Pt capsules were filled with MI-bearing olivines with and without de-ionised water and held at ~ 4 kbar and temperatures of 1250, 1280, and 1330 °C for ten minutes (supplement).

3.2. FTIR – glasses

H₂O and CO₂ MI concentrations ($n = 36$) were measured on the

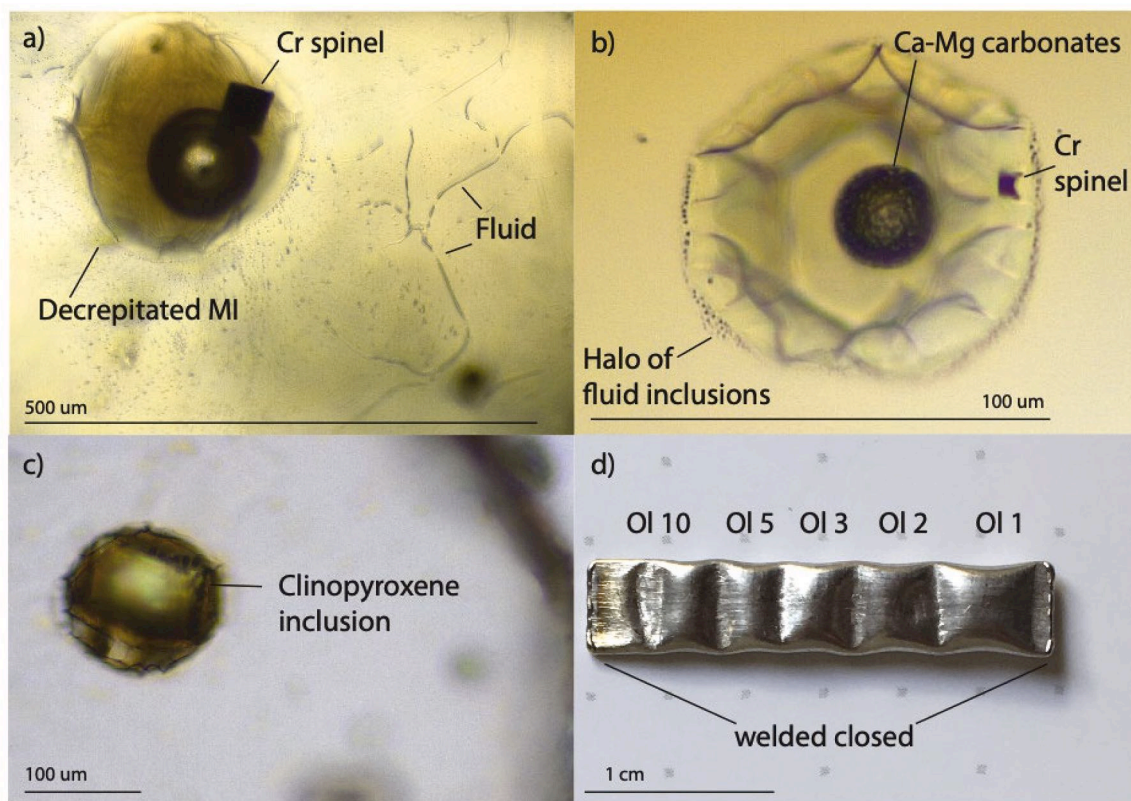


Fig. 2. (a) Decrepitated MI containing a Cr-spinel with fluid inclusions radiating away from the MI along a planar crack. Note the large bubble size, which is a feature of these decrepitated MIs. (b) Typical Etna FS MI containing tiny Cr-spinel and vapor bubble lined with Ca-Mg carbonates. Photo is looking down **b**. The halo of tiny fluid inclusions around the MI is ubiquitous in this sample. (c) Inclusion of melt and clinopyroxene within olivine. (d) capsule for IHPV experiments. Individual olivines are separated by gently crimping around them in order to compare before and after photos.

Thermo Nicolet iN10 at Lamont-Doherty Earth Observatory. We paid particular attention to the baseline under the carbonate peaks (Shi et al., 2024). Full details are in the supplement.

3.3. FTIR – olivine

H₂O concentration profiles ($n = 18$) were measured in doubly polished olivine wafers on the Thermo Nicolet iN10 at Lamont-Doherty Earth Observatory (Fig. 3). Barth et al. (2023) found good agreement between different peak-specific diffusivities so we consider bulk H₂O by summing the total area under the baseline-subtracted spectra. Full details are in the supplement.

3.4. SIMS

Rehomogenized MIs were fragile and developed cracks when intersected by polishing. Therefore, FTIR was not an option for the rehomogenized MIs, which were singly polished and analyzed by SIMS. Volatile abundances in rehomogenized MIs ($n = 26$) were measured using a Cameca IMS 1280 multi-collection ion microprobe at CRPG-CNRS-Nancy. The calibration for C during this session was noisy and deviated significantly from typical calibration curves for the same instrument (Supplementary data table). To check the calibration, one rehomogenized MI and two check standard glasses were removed from the indium mount, doubly polished, and measured by FTIR. These values were then used as the calibration line (Supplementary data table). A second SIMS session was conducted at Caltech in 2022, primarily to verify the H₂O data, and a reasonably good agreement was found (Supplementary data table).

3.5. EPMA

Major elements for MIs and adjacent spots in their host olivines ($n = 49$) were collected by electron microprobe analysis (EPMA) at the Smithsonian Institution using a JEOL JXA-8530F Hyperprobe. Major, minor and trace element profiles in olivine ($n = 8$) were measured using EPMA by a Cameca SX-5 with 5 WDS spectrometers at the American Museum of Natural History (AMNH).

3.6. Diffusion modeling – H₂O

In order to determine magma ascent rates, we performed diffusion modeling of H₂O concentration profiles in olivines, which is sensitive to ascent rate in the depth region in which H₂O is degassing from the magma (~0–15 km depth). Our methods mostly follow those in Newcombe et al. (2020), except that we do not fix the final (shallowest) pressure. Instead, we solve for both the best-fit decompression rate and final pressure. Full details are in the supplement.

3.7. Diffusion modeling – forsterite

To estimate timescales of ascent from storage to eruption, we performed diffusion modeling of forsterite in eight unhomogenized olivine crystals. All profiles show a decrease from a central plateau towards the rim over a lengthscale of 50 – 100 μm for all analyzed elements (Ni, Mn, Ca, Al, forsterite), regardless of their diffusivity (Fig. 4). Al is considered to be almost immobile in olivine at magmatic temperatures over timescales of decades (Spandler and O'Neill, 2010), while Ni, Mn, Ca and Fe-Mg all diffuse faster. Thus, the lack of decoupling between elements

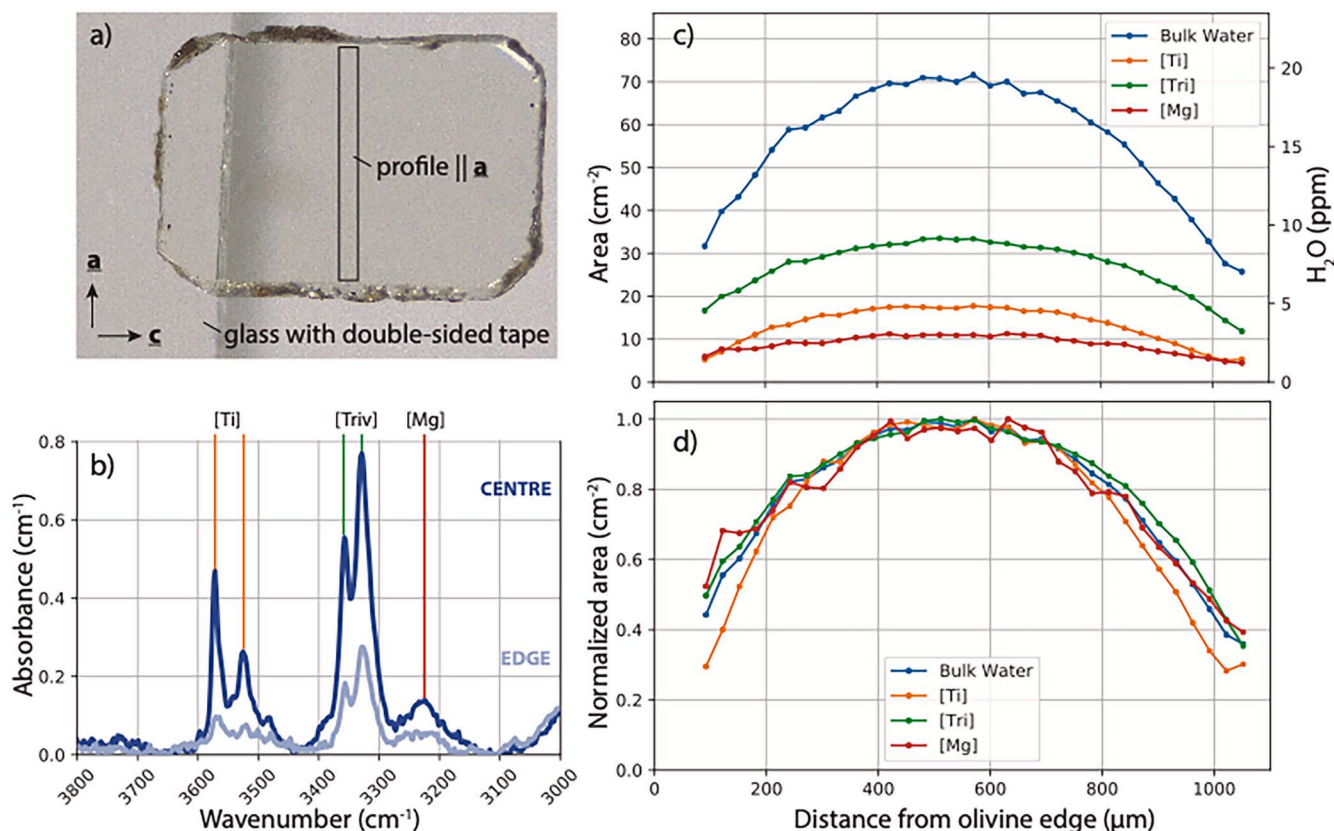


Fig. 3. H₂O concentration profile in olivine along the crystallographic a direction measured with FTIR. (a) Photograph of olivine wafer taken down b [010]. (b) FTIR spectra with baseline subtracted taken in the centre (dark blue) and edge (light blue) of the olivine. Absorption peaks represent OH⁻ bonds associated with different point defects. Bulk H⁺ concentration estimated by summing area under spectra from 3600 – 3100 cm^{-1} . (c) Defect-specific profiles along crystallographic a direction. Area is converted to H₂O concentration using the Withers et al. (2012) calibration and multiplying by a correction factor to account for the light which would be absorbed in the direction of the raypath. (d) Normalised defect-specific profiles.

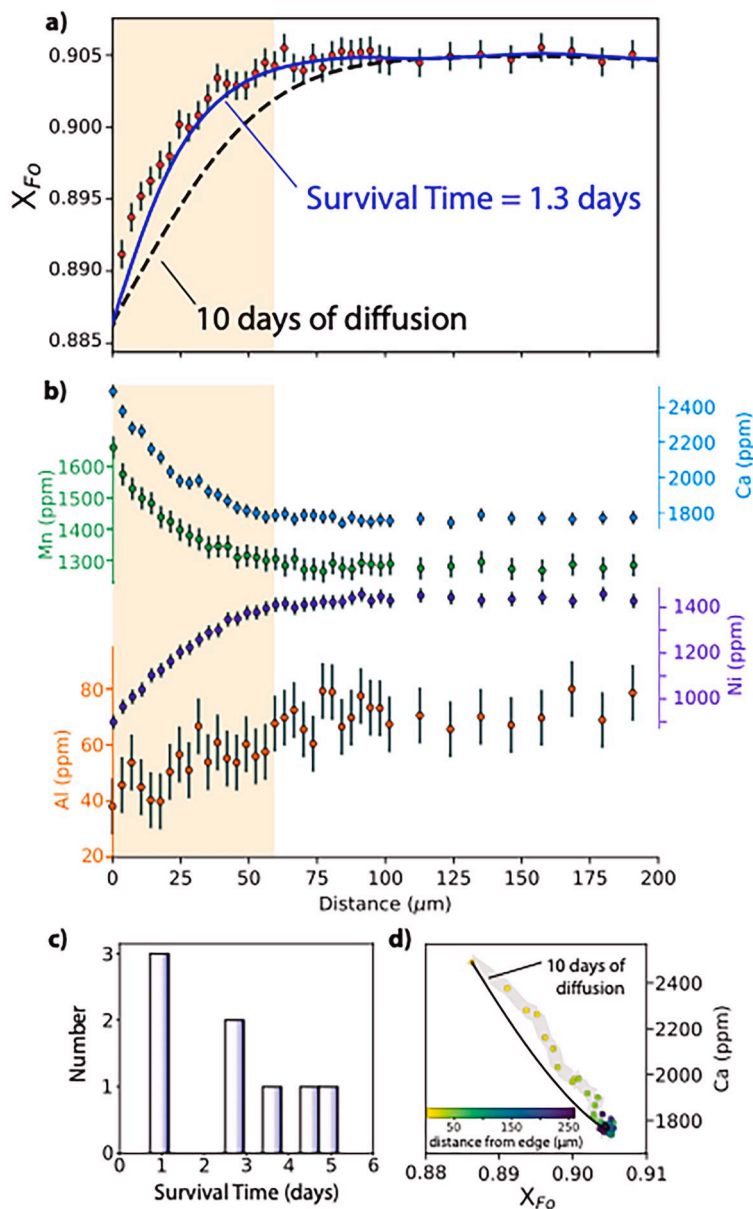


Fig. 4. a, b) Major and trace element diffusion profiles in one olivine (Ol52) along [001], the fast direction for Fe-Mg diffusion. Note the similar lengthscales of zonation profiles for all elements (shaded region), regardless of their diffusivity. c) histogram of survival times based on forsterite zonation profiles (see text for description of calculation). d) Initial condition for Fo diffusion modeling calculated from linear relationship between Fo and Ca. Black reference curve in a) and c) shows effect of 10 days of diffusion.

indicates that the zoning we observe was dominantly generated by crystal growth, and that there was insufficient time to modify these profiles by diffusion. Furthermore, due to diffusive anisotropy in olivine, where Fe-Mg interdiffusion is 6 times faster along the \underline{c} than the \underline{a} axis (Dohmen and Chakraborty, 2007), we would expect to see different diffusive lengthscales along different crystallographic directions. The similar zoning lengthscales of forsterite content along \underline{a} and \underline{c} also argues for growth-dominated zoning.

We used a combination of forward and inverse modeling to obtain the maximum timescale in which Fe-Mg growth-zoning can be preserved for each measured profile along the \underline{c} axis (supplement). This would give the maximum residence time at magmatic temperatures between crystal entrapment near the Moho and quenching upon eruption. To calculate this diffusive decoupling timescales for Fe-Mg interdiffusion, we used the measured growth profile as the initial condition. This assumes that the whole rim grew instantaneously, where the start of the growth rim is marked by the decrease of Al from core values. We then modeled Fe-Mg

diffusion until the model curve can be considered sufficiently decoupled from the initial growth conditions, accounting for analytical uncertainty. Modeling was performed using DFENS (Mutch et al., 2019, 2021) – full details in the supplement.

4. Results

4.1. IHPV rehomogenization experiments

After ten minutes of heating at 1250, 1280, and 1330 °C in the IHPV, the MIs exhibit a range of textures. All MIs become darker-colored after heating (Fig. 5), which may reflect the presence of Fe-bearing nanolites or an increased $\text{Fe}^{3+}/\Sigma\text{Fe}$ (Lerner et al., 2021). Some MIs are glassy and still contain a single vapor bubble, although comparing photos taken before and after the experiment shows that the bubbles have shrunk and moved during the experiment (Fig. 5a,b). Some MIs become very dark and speckled (with μm -scale bubbles or crystals) throughout (Fig. 5i,j),

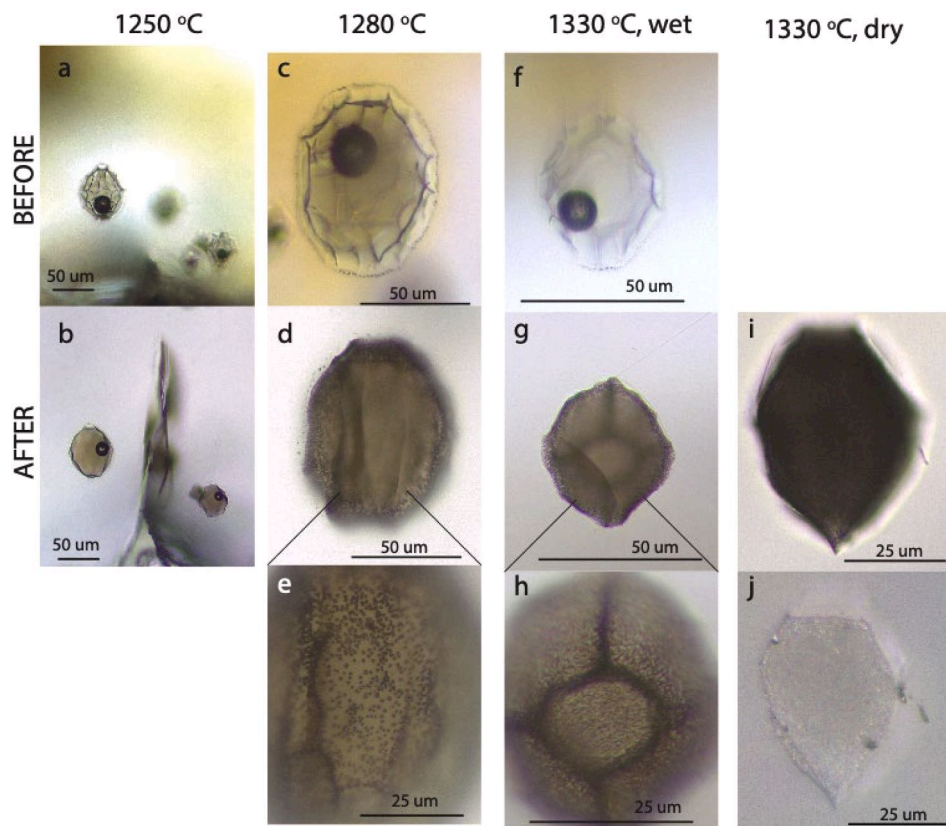


Fig. 5. Before and after photographs of MIs at different experimental temperatures and conditions. There was no ‘before’ photo for the MI heated in dry capsule at 1330 °C. (a) and (b) show photos of MIs before and after heating at 1250 °C under wet conditions. Note the MI color becomes darker, the faceting less distinct, the carbonate lining the bubble dissolves, and the bubble shrinks and moves. (c) and (d) show photos for MI before and after heating at 1280 °C under wet conditions. Bubble is fully dissolved and MI interior is glassy. (e) Photograph focused on bottom surface of MI and zoomed in to show tiny bubbles and/or crystals lining MI wall. (f–h) are same as (c–e) but for 1330 °C. (i) and (j) show transmitted and reflected photographs of MI heated at 1330 °C under dry conditions. MI becomes dark and speckles can be seen in reflected light throughout interior of MI.

while others are glassy inside but have speckled surfaces (Fig. 5c–h).

For further analysis, MIs which had resorbed their bubble were prioritized – no MIs at 1250 °C, and only two MIs at 1280 °C (OI8, OI29) were chosen. All available MIs from the 1330 °C runs were analyzed.

4.2. Major and minor elements

The measured chemical compositions of the MIs and their host olivines agree well with those of Kamenetsky et al. (2007), Corsaro and Métrich (2016), and Gennaro et al. (2019) (Fig. 6). We correct for PEC using MIMiC (Rasmussen et al., 2020) calculating the partition coefficient, K_d , from Toplis (2005) fixing Fe^{3+}/Fe_T to 0.32 based on micro-XANES measurements in Gennaro et al. (2020).

These calculations suggest minor PEC – up to 8%, with an average of 3%. Several MIs appear to have excess olivine – a possible sign of reheating. MIs show a limited range in all major and minor elements, and host olivine forsterite contents are equally restricted (90.3 – 91.2%) – there is no evidence for significant fractionation (Fig. 6). Entrapment temperatures calculated from MIMiC are 1196 ± 11 °C (supplementary data table).

One remarkable characteristic of the Etna FS MIs is their extremely low Al_2O_3 (9.1 – 11. wt%) and high CaO (13.5 – 15.5 wt%) concentrations. While low Al_2O_3 can be achieved by high pressures of melting, the combination of high CaO and low Al_2O_3 points to a high CO_2 concentration in the source (Dasgupta et al., 2007; Lara and Dasgupta, 2022) or the involvement of clinopyroxene reaction processes (Danyushevsky et al., 2004).

The homogenized MIs show evidence for significant melting of the

olivine host, as well as Fe-Mg exchange (MgO concentrations up to 18.5 wt%), which is common in these types of experiments that overheat the MIs (e.g. Rasmussen et al. 2020). When they are corrected for these processes, they overlap with the compositions of the unhomogenized MIs (Fig. S6).

4.3. Volatiles

Unhomogenized MIs show a weak positive correlation between H_2O and CO_2 with ranges of 2.5–4.9 wt% and 1910–3190 ppm, respectively (Fig. 7c). After PEC correction, these values are slightly lower due to the effect of dilution and are in the range 2.3–4.9 wt% and 1890–3110 ppm. In agreement with Gennaro et al. (2019), we do not find a correlation between H_2O concentrations and MI size (Fig. 7d, see supplement for details on size calculation), suggesting that the MIs have not undergone significant water loss during ascent (e.g. Qin et al. 1992). FTIR values for H_2O and CO_2 overlap with those in Gennaro et al. (2019), although their SIMS measurements are offset to higher concentrations for both volatiles (supplement).

Homogenized MIs show a range of CO_2 concentrations from 4900 to 9600 ppm – a clear increase from the unhomogenized MIs (Fig. 7c) that is on average two-fold. Four of the measured MIs have a single remaining vapor bubble, and these MIs fall to the low end of the range of CO_2 concentrations (open black circles, Fig. 7c). Nine homogenized MIs contain multiple small bubbles at their edge; however, this does not appear to affect their CO_2 concentrations (purple vs. red circles, Fig. 7c), as found in Rasmussen et al. (2020). All of the homogenized MIs have μm -scale phases (crystals and/or bubbles), primarily lining the MI wall,

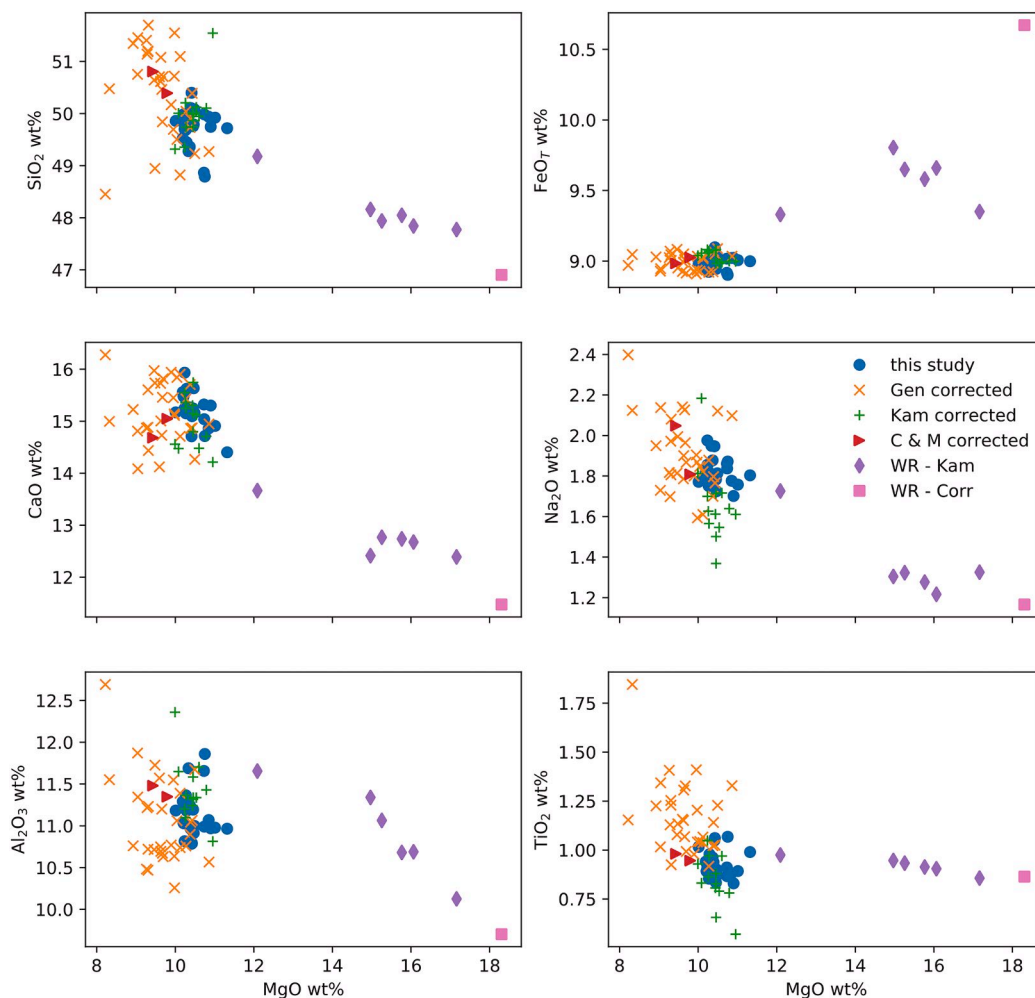


Fig. 6. PEC-corrected major element composition of unheated MIs from this study (blue circles). Data from literature for Etna FS shown for comparison (Gennaro et al., 2019), orange crosses; (Kamenetsky et al., 2007), green plus; (Corsaro and Métrich, 2016, red triangle). Whole rock (WR) from Kamenetsky et al. (2007) (purple diamond) and Corrales et al. (2014) (red square) and shows variable degrees of crystal accumulation. All data is normalized to 100% volatile-free. Note that data for other MI studies was corrected for PEC using MIMiC with the same parameters as the data in this study (see supplementary data table).

but in some cases distributed in the interior of the MI. At present, we do not know what these phases are, and it is possible that they contain some CO_2 , which would make our measurements lower bounds on the total amount of CO_2 in the MIs. Furthermore, the ‘haloes’ of secondary fluid inclusions surrounding all inclusions even before homogenization (Fig. 2) may indicate partial decrepitation, in which case the amount of CO_2 in the MIs at the time of entrapment may have been higher still.

Homogenized MIs have a narrower range and higher H_2O concentrations than unheated (Fig. 7c). This is unlikely to be the result of H_2O diffusing through the olivine from the experimental capsule since the experiments only last ten minutes, and we observe no systematic difference between dry and wet experiments. We cannot rule out that this is an analytical discrepancy – three unhomogenized and one homogenized MIs were measured by both SIMS and FTIR and the methods show discrepancies up to 0.85 wt.%, with the FTIR values exhibiting a wider range than the SIMS (supplement). It is possible that the FTIR measurements on unheated MIs underestimate H_2O concentration due to saturation of the detector. However, this would not explain the observed (albeit weak) H_2O - CO_2 correlation (Fig. 7c). Furthermore, we would expect the thickest wafers to give the lowest H_2O values, which is not observed (Fig. S3). Alternatively, there may be hydrous phases on the walls of the MIs (although we note that none were found by Raman spectroscopy – Kamenetsky et al. 2007) or H_2O in the vapor bubble prior to homogenization, which is added back into the melt during

homogenization (Esposito et al., 2016; Portnyagin et al., 2007).

The homogenization experiments do not appear to have altered the MI S or Cl concentrations (Fig. 7e), suggesting that they are not stored in the vapor bubble in significant quantities. In agreement with the results of Gennaro et al. (2019) and Corsaro and Métrich (2016), we find that S does not correlate with CO_2 or H_2O , although it strongly correlates with Cl for both the homogenized and unhomogenized MIs (Fig. 7e–g). The S-Cl correlation is surprising since Cl and S are not expected to degas at such high pressures (> 500 MPa) (e.g. Ding et al. 2023). Neither correlate with Ni or Fo of the host olivine, or any indices of fractionation (e.g. K_2O). Cl and S variations may thus be indicative of primary melt heterogeneity (as is present in other trace elements – Kamenetsky et al. 2007).

4.4. Diffusion modeling

4.4.1. H_2O

All olivines appear zoned in H_2O concentration along a with no central plateaus, indicating that diffusion has reached the center of each olivine. Central H_2O concentration ranges from 14 to 33 ppm. Edge concentrations range from 6 to 25 ppm. An example Monte Carlo model run can be seen in Fig. 8. There is a positive correlation between the diffusivity and decompression rate while other parameters exhibit weak or no correlation with decompression rate. Therefore, within the

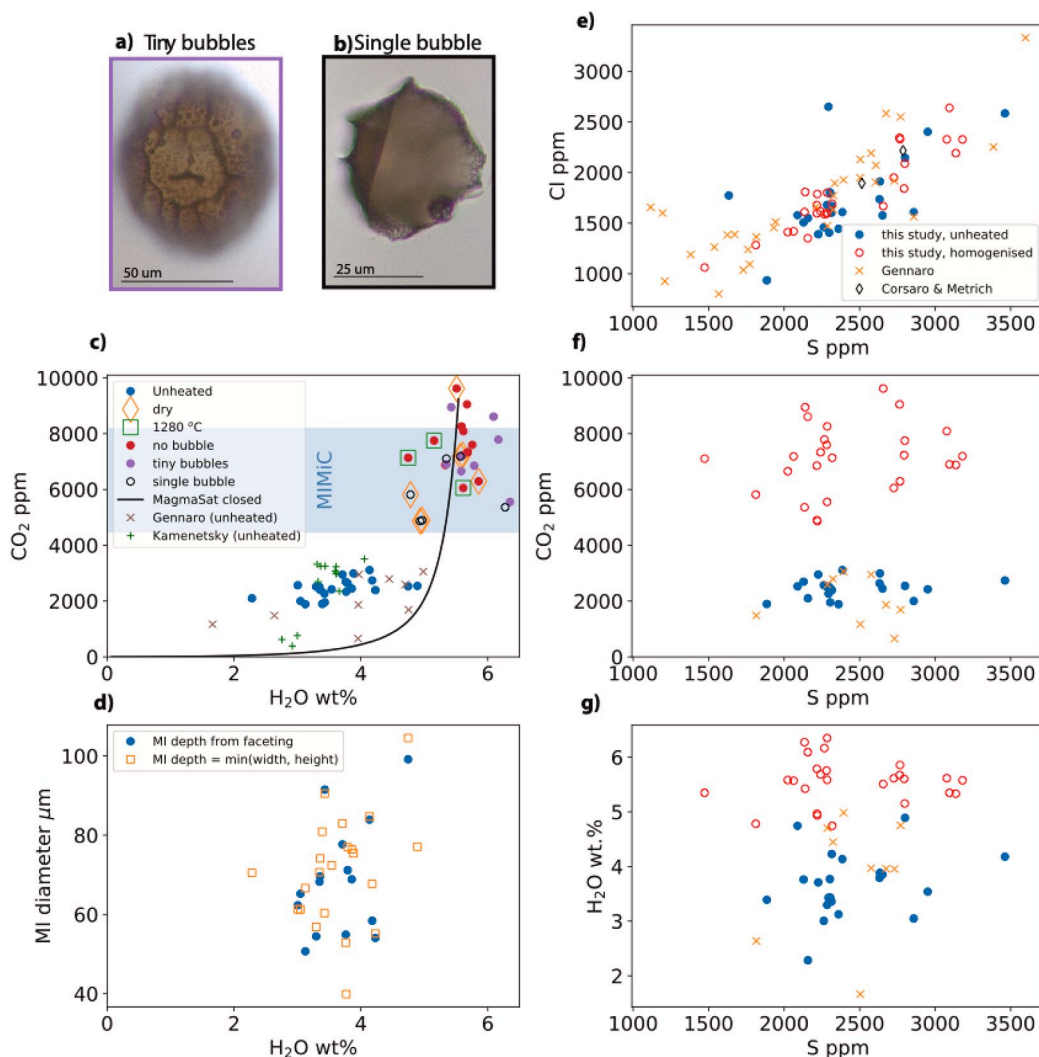


Fig. 7. Volatiles in homogenized and unheated MIs. (a, b) Examples of MIs with a single vapor bubble and multiple tiny bubbles. (c) H₂O versus CO₂ for homogenized and unheated MIs. Dry experiments shown with orange diamonds. Experiments at 1280 °C shown with green squares (all others are at 1330 °C). MIs with a single vapor bubble (open circles) plot to lower CO₂ concentrations. However, MIs with multiple tiny bubbles (purple circles) do not have less CO₂ than those without (red circles). Note that unheated MIs show scattered positive trend. CO₂ predicted by MIMiC modeling of unheated MIs (shaded blue) is similar to measurements of homogenized MIs. MagmaSat closed system degassing trend used in diffusion modeling of H^+ in olivine profiles is overlain. (d) H₂O versus MI diameter measured from photographs in two ways for unheated MIs. The first method is detailed in the supplement and uses MI faceting to predict MI depth from photographs taken down the \underline{b} axis (blue circles). This method is only possible for MIs which were photographed down the \underline{b} axis. The second method assumes that MI depth is equal to the shortest MI dimension measured in the photograph (orange squares). (e) Cl versus S measured by EPMA. Note the strong, approximately linear, correlation between S and Cl in all three studies (Gennaro et al., 2019; Corsaro and Métrich, 2016; this study), and for both unheated and homogenized MIs. (f) CO₂ versus S, symbols same as in (e). CO₂ measured by FTIR for unheated MIs and SIMS for homogenized MIs. (g) H₂O versus S, symbols same as in (e). Note that for data from Gennaro et al. (2019), only H₂O and CO₂ determined by FTIR are shown.

parameter ranges studied here, the uncertainty in diffusivity accounts for the largest source of uncertainty in decompression rate. We emphasize, however, that the diffusivity used was determined specifically for Etna FS olivines in a companion study (Barth et al., 2023). The best-fit decompression rate for all 18 olivines is remarkably uniform (Fig. 8b). A histogram of all best-fit decompression rates shows a lognormal distribution centered at 0.47 MPa/s with 95% confidence bounds of 0.16 and 1.28 MPa/s. Assuming an average crustal density from the surface to 15 km depth of 2600 kg/m³ from Corsaro and Pompilio (2004), this corresponds to 17.5 m/s with 95% confidence bounds of 6 and 49 m/s.

4.4.2. Forsterite

The median diffusive decoupling timescales determined from the Bayesian inversion (Mutch et al., 2021) range from one to five days for the different olivines. Uncertainties on these timescales propagated from

those in temperature, fO_2 , pressure, and diffusion coefficients vary for the different olivines and are -2 days and $+4$ days on average (full results in supplementary data table). Note that we can only constrain an upper bound on timescales since there are no diffusion profiles to model.

These results indicate that the olivines must have ascended from storage at near Moho depths to the surface at rates of 0.05 – 0.35 m/s or faster. If ascent were slower, the olivines would show signs of reequilibration with the surrounding olivine-free granulitic crust (Corsaro and Pompilio, 2004; Tonarini et al., 1996). Recent experimental results from Shea et al. (2023) show that the presence of a surrounding melt may enhance cation diffusion in olivines by up to a factor of 10. While the mechanism for this effect is still not well understood, it is thus possible that the true ascent velocities are even faster than the above estimates.

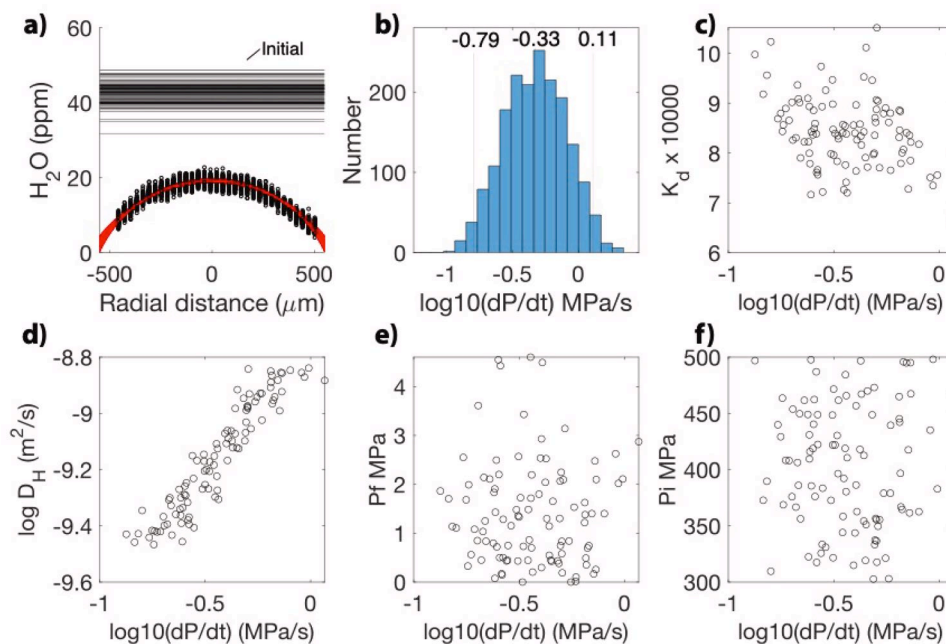


Fig. 8. Example Monte Carlo run to constrain decompression rate and final pressure by modeling 1D H^+ diffusion along crystallographic a direction. (a) FTIR profile with noise added in black circles, model fits (red lines). Initial H_2O concentration chosen from normal distribution with mean of 42 ppm and standard deviation of 3 ppm. (b) Histogram of best-fit decompression rates for all Monte Carlo runs for different olivines. Vertical lines show mean and 95% confidence intervals (c) Partition coefficient, K_d , versus decompression rate. K_d is calculated as the ratio of initial H_2O concentration in olivine (shown in (a)) relative to magma, which is set by MagmaSat solubility model and initial pressure, P_i . (d) Diffusivity versus decompression rate shows a clear positive correlation – most of the uncertainty in decompression rate comes from uncertainty in diffusivity. Upper bound of diffusivity is set by fastest dehydrating rate measured (Ferriss et al., 2018), Lower bound is set by initial dehydration rate measured in Barth et al. (2023). Final, P_f , (e) and initial, P_i , (f) pressure versus decompression rate show no relationship. Range of initial pressure chosen as the region in which H_2O begins significant degassing.

5. Discussion

5.1. Reconstructed CO_2 concentrations

5.1.1. Comparison of MIMiC and homogenization experiments

Since the discovery of the importance of MI vapor bubbles, several methods have been developed to account for the CO_2 stored within them. These techniques fall broadly into three categories: (1) dissolving the vapor bubble back into the MI with rehomogenization experiments before measurement, (2) using an equation of state and measuring or modeling the size of the bubble, and (3) measuring the CO_2 in the vapor bubble with Raman spectroscopy. These methods are described and compared more fully elsewhere (Moore et al., 2015; Rasmussen et al., 2020; Wallace et al., 2021). We compare the results of our rehomogenization experiments with the modeling approach of Rasmussen et al. (2020) using the publically available MIMiC code. MIMiC calculates bubble volume at the closure temperature for CO_2 (the temperature at which CO_2 diffusion effectively ceases), using an equation of state approach, and taking into account deformation of the host olivine. The model input includes the measured chemistry and sizes of the MIs and olivine hosts and an estimate of cooling rate (we assume a cooling rate of $10^\circ C/s$, as recommended for lapilli-sized clasts – Rasmussen et al. 2020).

There is close agreement between the CO_2 concentrations predicted by MIMiC using the unheated MIs and those measured by SIMS in the homogenized MIs, giving a spread of 4400–8200 and 4900–9600 ppm, respectively (Fig. 7c). This suggests that minimal CO_2 is stored in the tiny phases lining the walls of some of the rehomogenized MIs (Fig. 7a, b).

5.1.2. Pressure of magma storage

One of the primary ways to estimate magma storage depth is by calculating saturation pressures based on the H_2O and CO_2

concentrations within MIs. Therefore, restoring the CO_2 concentrations in the vapor bubbles has implications for the depths of magma storage. Note that these pressures are minima because they assume that the magma is saturated with a H_2O - CO_2 vapor phase. There are a range of solubility models for mixed volatiles, which have been calibrated over different pressure, temperature, and compositional space. MagmaSat (Ghiorso and Gualda, 2015) has the best coverage near the Etna FS composition and temperatures (Figs. S4,5). Duan (2014) also has good coverage, although is not implemented in the python package VESical (Iacovino et al., 2021). The models from Iacono-Marziano et al. (2012), Allison et al. (2019), and Allison et al. (2022) are calibrated on Etna magma but because the FS magma is so unusual for Etna it lies outside their compositional range (Figs. S4,5). The model of Dixon (1997) has good compositional coverage but does not extend to pressures higher than 500 MPa, and Iacono-Marziano et al. (2012) suggested that the Dixon (1997) calibration range was only reliable up to 100 MPa.

MagmaSat and Duan (2014) give the highest saturation pressures (676–819 and 787–1032 MPa, respectively), corresponding to the range in CO_2 concentrations in homogenized MIs without single vapor bubbles), while the solubility models in Iacono-Marziano et al. (2012), Allison et al. (2019), and Allison et al. (2022) give lower pressures (405–524, 415–649, and 343–547 MPa, respectively). Based on the different lithologies with depth beneath Etna (Corsaro and Pompilio, 2004), we iteratively solve for the magma storage depth and average density of the overburden. This gives an average overburden density of 2720 kg/m^3 and depth of 30 km for the highest initial pressure of 819 MPa, and average density and depth of 2650 kg/m^3 and 24 km for the shallowest initial pressure of 676 MPa. These depths closely align with entrapment depths determined from olivine-hosted CO_2 -rich fluid inclusions of 21–24 km of samples from Aci Castello and Mt. Maletto (Kamenetsky and Clocchiatti, 1996). We now examine how these depths relate to the crustal structure beneath Etna.

Although the regional Moho beneath eastern Sicily is on the order of

30 km (e.g. [Accaino et al. 2011](#)), detailed seismic imaging offshore of Etna finds a mantle upwarp ([Nicolich et al., 2000](#)) associated with a major tectonic feature, the Alfeo Fault System ([Dellong et al., 2018](#)). [Nicolich et al. \(2000\)](#) map a thinning of the Moho from 25 to 17 km immediately offshore of Etna, and suggest that the location of Etna is related to this tectonic feature. We thus consider the Moho beneath Etna to be in the range of 17–25 km and that the FS magma ascended from storage at or beneath the Moho. Viewed another way, our volatile saturation pressures can help to constrain the Moho depth, since the high and uniform forsterite content (90–91) of the FS olivines requires that the olivines must be coming from storage at or below the Moho, since they cannot have equilibrated with the olivine-free mafic granulites of the lower crust ([Corsaro and Pompilio, 2004](#); [Tonarini et al., 1996](#)). As noted by [Corsaro and Pompilio \(2004\)](#) the FS magma “represents a primitive melt in equilibrium with the mantle”. Crucially, the entrapment depths of the FS MIs means that the high CO₂ concentrations cannot have been the result of assimilation of the shallow carbonate crust, which is thought to extend to depths of ~ 10 km ([Fig. 9, Corsaro and Pompilio, 2004](#)).

5.2. Carbonate in the mantle source feeding the FS eruption

Here, we address the question of what generated the unusually high CaO/Al₂O₃ ratios (1.1–1.5) in Etna FS MIs and whole rocks ([Fig. 10, Kamenetsky et al., 2007](#); [Corsaro and Métrich, 2016](#)). The two primary hypotheses are involvement of 1) clinopyroxene-bearing lithologies or 2) carbonate in the magma’s source.

High CaO MIs have been explained by melting/dissolution of clinopyroxene-bearing lithologies in general terms ([Danyushevsky et al., 2004](#); [Schiano et al., 2000](#)) and specifically for the Etna FS magma ([Correale et al., 2014](#); [Corsaro and Métrich, 2016](#)). However, the approach of [Correale et al. \(2014\)](#) relied on assumptions about melting and crystallization based on major element modeling which was not able to fit the FS compositions (see their [Fig. 10](#)). [Corsaro and Métrich \(2016\)](#) argue that the high Zr/Nb and low Ce/Y requires the melting of a

clinopyroxene-bearing lithology, however measured ratios in FS whole rocks overlap with measured ratios for Hyblean peridotite xenoliths ([Correale et al., 2014](#)).

On the other hand, experiments have shown that addition of CO₂ to the mantle source can generate high CaO/Al₂O₃ ratios in the magma (up to 2.7), both by lowering Al₂O₃ and raising CaO in the melt (e.g. [Dasgupta et al. 2007](#)). In volatile-free peridotite, this level of CaO-enrichment and Al₂O₃ depletion can only be generated by melting at pressures above 4–5 GPa ([Walter, 1998](#)) – greater than typical arc melting pressures. Recent experiments with H₂O- and CO₂-bearing fluids ([Lara and Dasgupta, 2022](#)) suggest that the Etna FS magma composition could be explained by the presence of a fluid with XCO₂ (molar CO₂/(CO₂+H₂O)) of ~ 0.1. Furthermore, the olivine compositions (namely their Ni, Mn, and Ca concentrations) are consistent with carbonate metasomatism of the magma’s source, rather than involvement of pyroxenite ([Fig. 10a; Ammannati et al., 2016](#)).

Finally, there is a regional signature of carbonate metasomatism in the mantle. At Stromboli volcano, 115 km from Etna, isotopically heavy C ($\delta^{13}\text{C}$ –2.7‰ to –1.0‰), indicative of carbonate, was measured in bulk separates of high forsterite olivines from xenoliths of ultramafic cumulates thought to derive from the mantle ([Gennaro et al., 2017](#)). The authors propose that this reflects contamination of the mantle by C-rich sediments from the subducting slab. Magmas from the Hyblean district, ~60 km S of Etna show trace element and Sr-Nd-Pb isotopic signatures consistent with carbonatite metasomatism (e.g. [Trua et al. 1998](#)). C-rich fluid inclusions in wehrlitic xenoliths from Monte Vulture (~350 km N of Etna) further support carbonate metasomatism of the mantle ([Carnevale et al., 2022](#)). Below, we outline further support for the involvement of C-rich subducting sediments in the source of the Fall Stratified eruption.

Etna is situated away from the main Aeolian arc, and its location may be related to a tear in the subducting slab (e.g. [Gvirtzman and Nur 1999](#)). A trace element subduction signature (enrichment in large-ion lithophile (LILE), depletion in high field strength elements (HFSE)) has been documented for Etna magmas since ~100 ka ([Corsaro and](#)

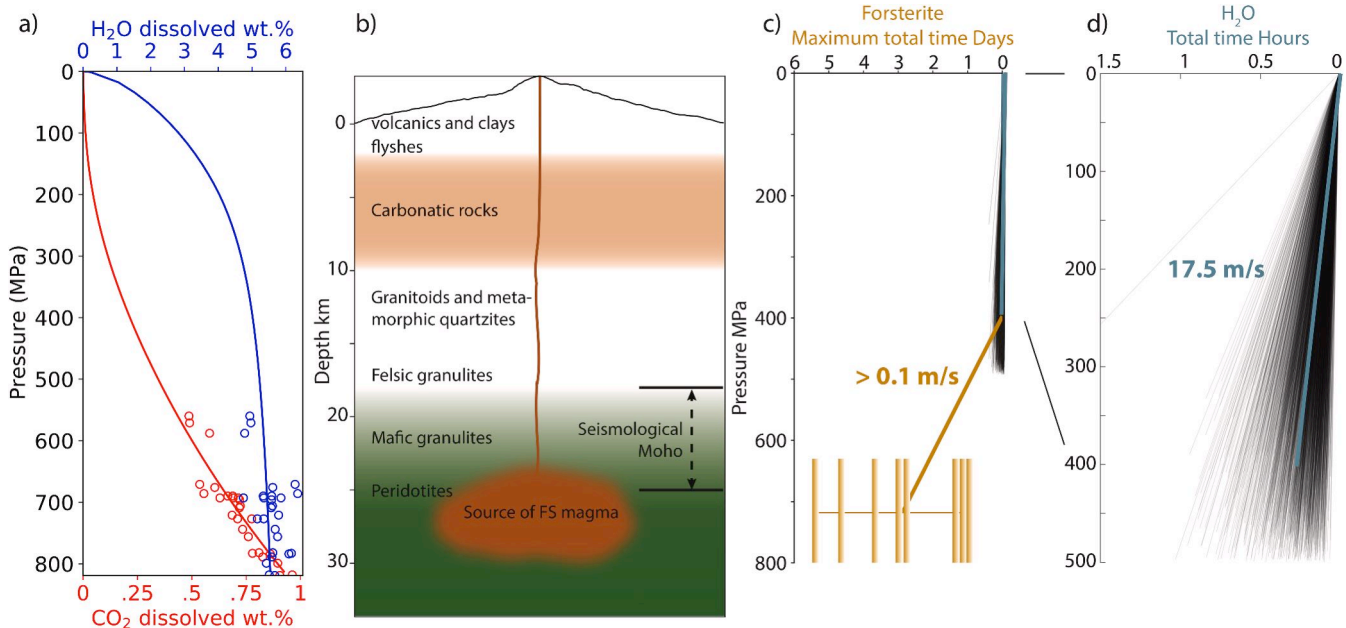


Fig. 9. a) Degassing path modeled with MagmaSat for FS magma with MI saturation pressures determined with MagmaSat ([Ghiorso and Gualda, 2015](#)) overlain in blue (H₂O) and red (CO₂) circles. Crustal section beneath Etna with lithologies from [Corsaro and Pompilio \(2004\)](#). Likely range of Moho depth from seismological observations shown by dashed arrow (see text for references). c) Maximum ascent times from storage to surface calculated from forsterite zonation modeling shown as vertical yellow bars. Vertical span of yellow bars represents uncertainty in storage pressure for range of MI volatile contents. Average ascent rate is 0.1 m/s and is shown by bold yellow line. Note that each bar represents a maximum, not best-fit, ascent time for one olivine. Ascent rate from H₂O Monte Carlo diffusion modeling shown by black lines, with mean ascent rate overlain in blue d) Zoom-in of H₂O diffusion model. Each black line represents results from a single Monte Carlo run. Average ascent rate is 17.5 m/s and is shown by bold blue line.

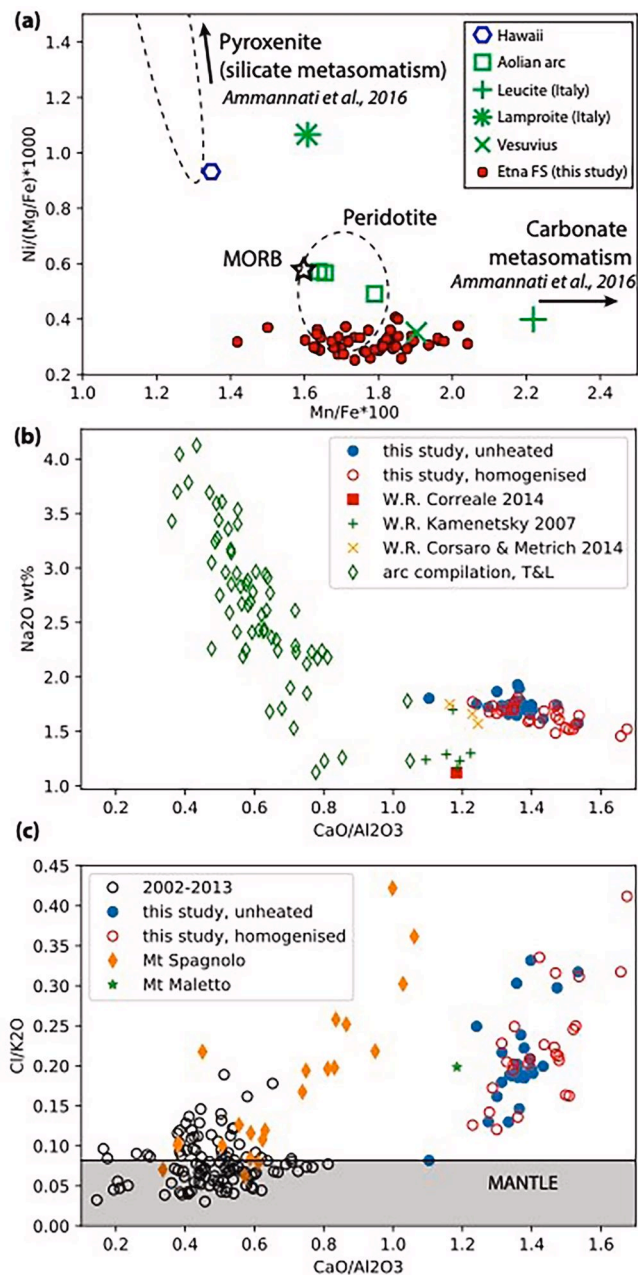


Fig. 10. Evidence for carbonate in FS magma source (a,b) and involvement of subducting slab(c). (a) Olivine compositions from FS have low Ni concentrations, prohibiting a large role for pyroxenite in its source. Compositions for other Italian magmas (green) from Zamboni et al. (2017). Also shown are the compositions for peridotite and pyroxenite, as well as the expected trend for silicate and carbonate mantle metasomatism from Ammannati et al. (2016). (b) Whole rock and melt inclusions (this study) of the FS magma is outside of the global arc array (from samples with $Mg\# > 60$, Turner and Langmuir, 2015) at low Na_2O and high CaO/Al_2O_3 . (c) Comparison of Cl/K_2O for modern eruptions and three primitive eruptions at Etna (Mt. Spagnolo – Gennaro et al. 2019, Mt Maletto – Schiano et al. 2001, and Fall Stratified – this study). Modern eruptions have only moderately higher Cl/K_2O ratios compared with MORB, and individual eruptions do not show a correlation between CaO/Al_2O_3 versus Cl/K_2O . In contrast, all three primitive eruptions have high Cl/K_2O and CaO/Al_2O_3 , and Mt. Spagnolo and FS show positive correlation between these ratios.

Métrich, 2016; Schiano et al., 2001; Tonarini et al., 2001), including for the FS magma (Kamenetsky et al., 2007). Using the average H_2O value from our MIs (~ 4.7 wt%) and the Ce concentration in the whole rock (Correale et al., 2014) and MIs (Kamenetsky et al., 2007) gives a H_2O/Ce

ratio of 750 and 500–1300, respectively – clearly above typical MORB values (100–300; Dixon et al., 2002), suggesting that a significant portion of the magma’s H_2O was derived from the subducting slab. Corsaro and Métrich (2016) show that the Cl/K_2O ratios of FS MIs are well above typical mantle values, suggesting that most of the Cl is derived from the slab (Fig. 10). High Cl/K_2O and CaO/Al_2O_3 ratios have also been found for other historical primitive eruptions at Etna: Mt. Spagnolo (15–4 ka) and Mt. Maletto (7 ka). Furthermore, Mt. Spagnolo and FS show a correlation between CaO/Al_2O_3 and degree of Cl enrichment. They are also the only two eruptions to show a positive correlation in S and Cl (supplement). Therefore, we propose that the high CaO/Al_2O_3 ratios and enrichment in Cl and S are reflecting a common process, likely input into the mantle of a fluid or melt that is rich in Cl, S, H_2O and CO_2 from a subducting slab, whether it was added just prior to the FS eruption or stored on long timescales in metasomatic phases in the mantle (Viccaro and Cristofolini, 2008).

5.3. Magma decompression rate

The combination of forsterite and H_2O diffusion modeling allows us to piece together the magma ascent rate all the way from source to surface (Fig. 9). The lack of diffusive zonation of forsterite within the olivine crystals is highly unusual and implies rapid ascent (> 0.1 m/s) from near Moho depths (24 – 30 km) to the surface in less than 1–5 days (Figs. 4 and 9). These rates are faster than those estimated for ascent from the Moho in the Borgarhraun eruption of Iceland (0.02–0.1 m/s; Mutch et al., 2019), which could be tied to the lower CO_2 concentrations (~ 600 ppm) and consequently shallower vapor saturation (~ 3 km) of the Borgarhraun magma.

The H_2O zonation profiles within the olivine crystals require average decompression rates of 0.47 MPa/s from depths of ~ 15 km to the surface. This is among the highest measured by diffusion chronometry for basaltic-intermediate eruptions (Barth et al., 2019; Cassidy et al., 2018), although faster rates have been found in the final few kilometers of ascent beneath Ambrym and Ambae/Aoba volcanoes (Moussallam et al., 2019; 2021) and for recent paroxysms at Etna (Giuffrida et al., 2018; Zuccarello et al., 2022). The most explosive of these recent paroxysmal events attained plume heights of ~ 15 km, although it was significantly lower in volume (by a factor of ~ 25 – Coltelli et al., 2005; Corsaro et al., 2017) and was sourced from shallower depths (~ 1 km b.s.l.) than the FS eruption. Crucially, the ascent rates that we determine exceed those which have been experimentally shown to induce CO_2 supersaturation, which has been suggested as a mechanism for fragmentation of low-viscosity basaltic magmas (Pichavant et al., 2013).

In keeping with the uniformity of olivine and MI compositions, the decompression rates are also highly uniform. This supports the observation by Newcombe et al. (2020) that more explosive eruptions may have less variable decompression rate than lower energy eruptions, for which unsteadiness in flow rate may be more pronounced.

To assess whether the ascent rates that we derive are physically plausible, we apply the analytical expressions for the propagation of fluid-filled fractures driven by fluid buoyancy given by Davis et al. (2023). In their formulation, ascent rate is a function of fluid volume, density, viscosity and the elastic parameters of the host medium. Using a Monte Carlo approach, we calculate ascent rate and uncertainty by drawing parameters from normal distributions (Fig. S10) with the following mean and standard deviation: volume = 0.055 ± 0.005 km³ (Coltelli et al., 2005), average density contrast between host crust and magma = 285 ± 100 kg/m³ (Fig. S9), and viscosity = 4.6 ± 0.5 Pa s (calculated from the model by Giordano et al. (2008) on the average unheated MI composition). Note that this viscosity model includes the effect of H_2O but not CO_2 , which could make the viscosity even lower (e.g. Di Genova et al. 2014). The Young’s modulus of the crust is the least well-constrained parameter; we calculate a depth-average from the surface to 30 km of 89 GPa from Currenti et al. (2007) and use a large uncertainty of ± 30 GPa. If ascent starts at 24–30 km depth, the model

predicts average ascent rates of 15–21 m/s (Fig. S11). This suggests that our calculated ascent rates from H₂O diffusion (mean of 17.5 m/s) and our lower bound from Fe-Mg interdiffusion (> 0.1 m/s) are reasonable.

5.4. Uniqueness of FS eruption

Other primitive Etna magmas (Mt. Spagnolo and Mt. Maletto) show similar geochemical characteristics as the FS magma (Corsaro and Métrich, 2016), implying that these magmas may not be rare at Moho depths beneath Etna but that their signature gets destroyed with mixing and fractionation in the plumbing system. Unlike the FS magma, Mt. Spagnolo and Mt. Maletto magmas both show a significant range in geochemical indicators of fractionation (e.g. K₂O, MgO), indicating that they either mixed with more fractionated magma during ascent, or crystallized extensively themselves. Either scenario implies slower ascent for these two magmas compared to the FS magma, which may have allowed the escape of their volatile phases and hence lowered the eruption intensity.

The high CO₂ concentration of the FS magma and a consequently deep exsolved vapor phase may have initiated diking at Moho depths. Thus, the magma was still hot and had low viscosity when it began ascending, allowing it to propagate fast (8–11 m/s, as above). Either the transporting dyke fortuitously avoided shallow magma reservoirs, or else it was able to pass through relatively unhindered, perhaps because of its fast speed and/or the long hiatus of volcanic activity that preceded the FS eruption (Fig. 1b), which may have allowed shallow magma bodies to cool and solidify. The total pressure-drop and vesicularity during ascent is thought to affect the expansion velocity of the magma, and consequently the eruptive intensity (e.g. Namiki and Manga 2006). Therefore, the FS magma's unhindered ascent from its deep storage pressures and its high volatile concentrations (particularly CO₂) may have been responsible for its high explosive energy. These conclusions mirror those of other recent studies that highlight the importance of CO₂ as a driver of explosive eruptions (Allison et al., 2021), some directly from the mantle (DeVitre et al., 2023).

6. Conclusions

The subplinian FS eruption of Etna was remarkable in terms of its primitive composition and high volatile concentrations. Previous studies underestimated the magma's CO₂ concentration by neglecting the MI vapor bubbles. In this study, we rehomogenized olivine-hosted MIs to resorb their vapor bubbles and carbonate back into the MIs. SIMS and FTIR measurements show that these rehomogenized MIs contain between 4900 and 9600 ppm CO₂, corresponding to magma storage pressures of at least 676–819 MPa (24–30 km). These depths are comparable to the seismologically estimated Moho (17–25 km) suggesting that MIs were entrapped in the mantle, and cannot have gained their CO₂ contents by dissolving the carbonate crust, which only extends to ~10 km depth. Instead, we argue that the MIs' high CO₂ concentration is derived from carbonate in the mantle source of Etna on the basis of MI CaO/Al₂O₃ ratios, olivine Ni contents, and isotopic measurements of C in high forsterite olivines from the nearby Stromboli volcano.

Diffusion modeling of H₂O and forsterite profiles in olivine crystals demonstrates the remarkably fast ascent of the FS magma. The forsterite profiles require that the magma ascended from near Moho depths to the surface in less than 1–5 days. Modeling H₂O profiles, which are sensitive to the region in which H₂O is degassing from the magma (<15 km depth), gives average decompression rates of 0.47 MPa/s or 17.5 m/s (assuming a lithostatic pressure gradient).

We propose that this eruption may record a link between the primary magma composition and eruption style; the unusually explosive nature of this picritic eruption was driven by the high CO₂ concentrations, imparted to the magma by subducted carbonate in the mantle source. This CO₂ caused deep exsolution of a vapor phase which may have initiated fast diking all the way from the Moho to the surface, relatively

uninterrupted by fractionation and mixing in the crust. The magma's deep origin, high volatile contents, and consequently rapid ascent, all acted to increase the explosive intensity of this eruption.

CRediT authorship contribution statement

Anna Barth: Writing – review & editing, Writing – original draft, Visualization, Validation, Project administration, Methodology, Investigation, Formal analysis, Data curation, Conceptualization. **Maxim Portnyagin:** Writing – review & editing, Validation, Methodology, Conceptualization. **Nikita Mironov:** Writing – review & editing, Validation, Methodology, Investigation, Conceptualization. **Francois Holtz:** Writing – review & editing. **Yves Moussallam:** Writing – review & editing, Formal analysis. **Estelle F. Rose-Koga:** Writing – review & editing, Formal analysis. **Daniel Rasmussen:** Writing – review & editing, Formal analysis. **Henry Towbin:** Writing – review & editing, Methodology, Investigation. **Helge Gonnermann:** Writing – review & editing, Investigation. **Euan J.F. Mutch:** Writing – review & editing, Methodology, Investigation, Formal analysis. **Silvio G. Rotolo:** Writing – review & editing, Resources, Investigation. **Terry Plank:** Writing – review & editing, Resources, Project administration, Investigation, Funding acquisition, Data curation, Conceptualization.

Declaration of competing interest

The authors declare that they have no known competing financial interests or personal relationships that could have appeared to influence the work reported in this paper.

Data availability

Data is in supplement and on GitHub, with link to GitHub in supplement.

Acknowledgements

The authors would like to thank Dave Walker for his help with the piston-cylinder experiments – his insight, intuition, and constant optimism were invaluable. We would also like to thank Philipp Beckmann for his help in performing the IHPV experiments, Yunbin Guan for making SIMS measurements at Caltech, and Céline Martin for microprobe measurements at AMNH. NM and FH acknowledge support from the joint DFG-RFBR project (HO1337/44-1, DFG to FH and 20-55-12013, RFBR to NM). EJFM acknowledges funding from a LDEO Postdoctoral Fellowship (UR005759). This work was funded by NSF grant number EAR-1524542 to TP.

Supplementary materials

Supplementary material associated with this article can be found, in the online version, at [doi:10.1016/j.epsl.2024.118864](https://doi.org/10.1016/j.epsl.2024.118864).

References

- Accaino, F., Catalano, R., Di Marzo, L., Giustiniani, M., Tinivella, U., Nicolich, R., Sulli, A., Valenti, V., Manetti, P., 2011. A crustal seismic profile across Sicily. *Tectonophysics* 508 (1–4), 52–61.
- Allison, C.M., Roggensack, K., Clarke, A.B., 2019. H₂O–CO₂ solubility in alkali-rich mafic magmas: new experiments at mid-crustal pressures. *Contrib. Mineral. Petrol.* 174 (7), 1–24.
- Allison, C.M., Roggensack, K., Clarke, A.B., 2021. Highly explosive basaltic eruptions driven by CO₂ exsolution. *Nat. Commun.* 12 (1), 1–10. <https://doi.org/10.1038/s41467-020-20354-2>.
- Allison, C.M., Roggensack, K., Clarke, A.B., 2022. MafiCH: a general model for H₂O–CO₂ solubility in mafic magmas. *Contrib. Mineral. Petrol.* 177 (3), 1–22. <https://doi.org/10.1007/s00410-022-01903-y>.
- Ammannati, E., Jacob, D.E., Avanzinelli, R., Foley, S.F., Conticelli, S., 2016. Low Ni olivine in silica-undersaturated ultrapotassic igneous rocks as evidence for carbonate

- metasomatism in the mantle. *Earth Planet. Sci. Lett.* 444, 64–74. <https://doi.org/10.1016/j.epsl.2016.03.039>.
- Anderson, A.T., 1995. CO₂ and the eruptibility of picrite and komatiite. *Lithos* 34 (1–3), 19–25.
- Anderson Jr, A.T., 1974. Evidence for a picritic, volatile-rich magma beneath Mt. Shasta, California. *J. Petrol.* 15 (2), 243–267.
- Bamber, E.C., Arzilli, F., Polacci, M., Hartley, M.E., Fellowes, J., Di Genova, D., Chavarría, D., Saballos, J.A., Burton, M.R., 2020. Pre-and syn-eruptive conditions of a basaltic Plinian eruption at Masaya Volcano, Nicaragua: the Masaya Triple Layer (2.1 ka). *J. Volcanol. Geotherm. Res.* 392, 106761.
- Barth, A., Newcombe, M., Plank, T., Gonnermann, H., Hajimirza, S., Soto, G.J., Saballos, A., Hauri, E., 2019. Magma decompression rate correlates with explosivity at basaltic volcanoes—Constraints from water diffusion in olivine. *J. Volcanol. Geotherm. Res.* 387, 106664.
- Barth, A., Plank, T., Towbin, H., 2023. Rates of dehydration in hydrous, high-Fo, magmatic olivines. *Geochim. Cosmochim. Acta* 342, 62–73.
- Branca, S., Del Carlo, P., 2005. Types of eruptions of Etna volcano AD 1670–2003: implications for short-term eruptive behaviour. *Bull. Volcanol.* 67 (8), 732–742.
- Carnevale, G., Caracausi, A., Rotolo, S.G., Paternoster, M., Zanon, V., 2022. New inferences on magma dynamics in melilitite-carbonatite volcanoes: the case study of Mt. Vulture (Southern Italy). *Geophys. Res. Lett.* 49 (21) <https://doi.org/10.1029/2022GL099075>.
- Cassidy, M., Manga, M., Cashman, K., Bachmann, O., 2018. Controls on explosive-effusive volcanic eruption styles. *Nat. Commun.* 9 (1) <https://doi.org/10.1038/s41467-018-05293-3>.
- Coltelli, M., Del Carlo, P., Pompilio, M., Vezzoli, L., 2005. Explosive eruption of a picrite: the 3930 BP subplinian eruption of Etna volcano (Italy). *Geophys. Res. Lett.* 32 (23), 1–4. <https://doi.org/10.1029/2005GL024271>.
- Coltelli, M., Del Carlo, P., Vezzoli, L., 1998. Discovery of a Plinian basaltic eruption of Roman age at Etna volcano, Italy. *Geology* 26 (12), 1095–1098. [https://doi.org/10.1130/0091-7613\(1998\)026<1095:DOAPBE>2.3.CO;2](https://doi.org/10.1130/0091-7613(1998)026<1095:DOAPBE>2.3.CO;2).
- Coltelli, M., Del Carlo, P., Vezzoli, L., 2000. Stratigraphic constraints for explosive activity in the past 100 ka at Etna Volcano, Italy. *Int. J. Earth Sci.* 89 (3), 665–677. <https://doi.org/10.1007/s005310000117>.
- Correale, A., Paonita, A., Martelli, M., Rizzo, A., Rotolo, S.G., Anna, R., Di, V., 2014. A two-component mantle source feeding Mt. Etna magmatism: insights from the geochemistry of primitive magmas. *Lithos* 184–187, 243–258. <https://doi.org/10.1016/j.lithos.2013.10.038>.
- Corsaro, R.A., Andronico, D., Behnke, B., Branca, S., Caltabiano, T., Ciancetto, F., Cristaldi, A., De Beni, E., La Spina, A., Lodato, L., Miraglia, L., Neri, M., Salerno, G., Scollo, S., Spata, G., 2017. Monitoring the December 2015 summit eruptions of Mt. Etna (Italy): implications on eruptive dynamics. *J. Volcanol. Geotherm. Res.* 341 (December 2015), 53–69. <https://doi.org/10.1016/j.jvolgeores.2017.04.018>.
- Corsaro, R.A., Métrich, N., 2016. Chemical heterogeneity of Mt. Etna magmas in the last 15 ka. Inferences on their mantle sources. *Lithos* 252–253, 123–134. <https://doi.org/10.1016/j.lithos.2016.02.006>.
- Corsaro, R.A., Pompilio, M., 2004. Buoyancy-controlled eruption of magmas at Mt Etna. *Terra Nova* 16 (1), 16–22.
- Currenti, G., Del Negro, C., Ganci, G., 2007. Modelling of ground deformation and gravity fields using finite element method: an application to Etna volcano. *Geophys. J. Int.* 169 (2), 775–786. <https://doi.org/10.1111/j.1365-246X.2007.03380.x>.
- Danyushevsky, L.V., Leslie, R.A.J., Crawford, A.J., Durance, P., 2004. Melt inclusions in primitive olivine phenocrysts: the role of localized reaction processes in the origin of anomalous compositions. *J. Petrol.* 45 (12), 2531–2553.
- Dasgupta, R., Hirschmann, M.M., Smith, N.D., 2007. Partial melting experiments of peridotite+ CO₂ at 3 GPa and genesis of alkalic ocean island basalts. *J. Petrol.* 48 (11), 2093–2124.
- Davis, T., Rivalta, E., Smittarello, D., Katz, R.F., 2023. Ascent rates of 3-D fractures driven by a finite batch of buoyant fluid. *J. Fluid Mech.* 954, 1–23. <https://doi.org/10.1017/jfm.2022.986>.
- Dellong, D., Klingelhoefer, F., Kopp, H., Graindorge, D., Margheriti, L., Moretti, M., Murphy, S., Gutscher, M.A., 2018. Crustal structure of the ionian basin and eastern sicily margin: results from a wide-angle seismic survey. *J. Geophys. Res. Solid Earth* 123 (3), 2090–2114. <https://doi.org/10.1002/2017JB015312>.
- DeVitre, C.L., Gazel, E., Ramalho, R.S., Venugopal, S., Steele-MacInnis, M., Hua, J., Allison, C.M., Moore, L.R., Carracedo, J.C., Monteone, B., 2023. Oceanic intraplate explosive eruptions fed directly from the mantle. *Proc. Natl. Acad. Sci.* 120 (33), e2302093120.
- Di Genova, D., Romano, C., Alletti, M., Misiti, V., Scarlato, P., 2014. The effect of CO₂ and H₂O on Etna and Fondo Riccio (Phlegrean Fields) liquid viscosity, glass transition temperature and heat capacity. *Chem. Geol.* 377, 72–86.
- Ding, S., Plank, T., Wallace, P.J., Rasmussen, D.J., 2023. Sulfur X: a model of sulfur degassing during magma ascent. *Geochem. Geophys. Geosyst.* 24 (4) e2022GC010552.
- Dixon, J.E., 1997. Degassing of alkalic basalts. *Am. Mineral.* 82 (3–4), 368–378.
- Dixon, J.E., Leist, L., Langmuir, C., Schilling, J.G., 2002. Recycled dehydrated lithosphere observed in plume-influenced mid-ocean-ridge basalt. *Nature* 420 (6914), 385–389. <https://doi.org/10.1038/nature01215>.
- Dohmen, R., Chakraborty, S., 2007. Fe-Mg diffusion in olivine II: point defect chemistry, change of diffusion mechanisms and a model for calculation of diffusion coefficients in natural olivine. *Phys. Chem. Miner.* 34 (6), 409–430. <https://doi.org/10.1007/s00269-007-0158-6>.
- Duan, X., 2014. A general model for predicting the solubility behavior of H₂O–CO₂ fluids in silicate melts over a wide range of pressure, temperature and compositions. *Geochim. Cosmochim. Acta* 125, 582–609.
- Esposito, R., Lamadrid, H.M., Redi, D., Steele-MacInnis, M., Bodnar, R.J., Manning, C.E., De Vivo, B., Cannatelli, C., Lima, A., 2016. Detection of liquid H₂O in vapor bubbles in reheated melt inclusions: implications for magmatic fluid composition and volatile budgets of magmas? *Am. Mineral.* 101 (7), 1691–1695.
- Gennaro, E., Grassa, F., Martelli, M., Renzulli, A., Rizzo, A.L., 2017. Carbon isotope composition of CO₂-rich inclusions in cumulate-forming mantle minerals from Stromboli volcano (Italy). *J. Volcanol. Geotherm. Res.* 346, 95–103. <https://doi.org/10.1016/j.jvolgeores.2017.04.001>.
- Gennaro, E., Iacono-Marziano, G., Paonita, A., Rotolo, S.G., Martel, C., Rizzo, A.L., Pichavant, M., Liotta, M., 2019. Melt inclusions track melt evolution and degassing of Etna magmas in the last 15 ka. *Lithos* 324–325, 716–732. <https://doi.org/10.1016/j.lithos.2018.11.023>.
- Gennaro, E., Paonita, A., Iacono-Marziano, G., Moussallam, Y., Pichavant, M., Peters, N., Martel, C., 2020. Sulphur behaviour and redox conditions in etnean magmas during magma differentiation and degassing. *J. Petrol.* <https://doi.org/10.1093/ptrology/egaa095>.
- Ghiorsio, M.S., Gualda, G.A.R., 2015. An H 2 O–CO 2 mixed fluid saturation model compatible with rhyolite-MELTS. *Contrib. Mineral. Petrol.* 169 (6), 1–30.
- Giordano, D., Dingwell, D., 2003. Viscosity of hydrous Etna basalt: implications for Plinian-style basaltic eruptions. *Bull. Volcanol.* 65 (1), 8–14. <https://doi.org/10.1007/s00445-002-0233-2>.
- Giordano, D., Russell, J.K., Dingwell, D.B., 2008. Viscosity of magmatic liquids: a model. *Earth Planet. Sci. Lett.* 271 (1–4), 123–134. <https://doi.org/10.1016/j.epsl.2008.03.038>.
- Giuffrida, M., Viccaro, M., Ottolini, L., 2018. Ultrafast syn-eruptive degassing and ascent trigger high-energy basic eruptions. *Sci. Rep.* 8 (1), 1–7. <https://doi.org/10.1038/s41598-017-18580-8>.
- Gvirtzman, Z., Nur, A., 1999. The formation of Mount Etna as the consequence of slab rollback. *Nature* 401 (6755), 782–785. <https://doi.org/10.1038/44555>.
- Houghton, B.F., Gonnermann, H.M., 2008. Basaltic explosive volcanism: constraints from deposits and models. *Chem. Erde Geochim.* 68 (2), 117–140. <https://doi.org/10.1016/j.chemer.2008.04.002>.
- Houghton, B.F., Wilson, C.J.N., Del Carlo, P., Coltelli, M., Sable, J.E., Carey, R., 2004. The influence of conduit processes on changes in style of basaltic Plinian eruptions: tarawera 1886 and Etna 122 BC. *J. Volcanol. Geotherm. Res.* 137 (1–3), 1–14. <https://doi.org/10.1016/j.jvolgeores.2004.05.009>. SPEC. ISS.
- Iacono-Marziano, G., Morizet, Y., Le Trong, E., Gaillard, F., 2012. New experimental data and semi-empirical parameterization of H₂O–CO₂ solubility in mafic melts. *Geochim. Cosmochim. Acta* 97, 1–23.
- Iacovino, C., Matthews, S., Wieser, P.E., Moore, G.M., Bégué, F., 2021. VESICAL Part I: an open-source thermodynamic model engine for mixed volatile (H₂O–CO₂) solubility in silicate melts. *Earth Space Sci.* 8 (11) e2020EA001584.
- Kamenetsky, V., Clocchiatti, R., 1996. Primitive magmatism of Mt. Etna: insights from mineralogy and melt inclusions. *Earth Planet. Sci. Lett.* 142 (3–4), 553–572. [https://doi.org/10.1016/0012-821x\(96\)00115-x](https://doi.org/10.1016/0012-821x(96)00115-x).
- Kamenetsky, V., Pompilio, M., Métrich, N., Sobolev, A.V., Kuzmin, D.V., Thomas, R., 2007. Arrival of extremely volatile-rich high-Mg magmas changes explosivity of Mount Etna. *Geology* 35 (3), 255–258. <https://doi.org/10.1130/G23163A.1>.
- Lara, M., Dasgupta, R., 2022. Carbon recycling efficiency in subduction zones constrained by the effects of H₂O–CO₂ fluids on partial melt compositions in the mantle wedge. *Earth Planet. Sci. Lett.* 588 <https://doi.org/10.1016/j.epsl.2022.117578>.
- Lerner, A.H., Muth, M.J., Wallace, P.J., Lanzirotti, A., Newville, M., Gaetani, G.A., Chowdhury, P., Dasgupta, R., 2021. Improving the reliability of Fe- and S-XANES measurements in silicate glasses: correcting beam damage and identifying Fe-oxide nanolites in hydrous and anhydrous melt inclusions. *Chem. Geol.* 586, 120610 <https://doi.org/10.1016/j.chemgeo.2021.120610>.
- McPhie, J., Walker, G.P.L., Christiansen, R.L., 1990. Phreatomagmatic and phreatic fall and surge deposits from explosions at Kilauea volcano, Hawaii, 1790 AD: keanakakoi Ash Member. *Bull. Volcanol.* 52, 334–354.
- Mironov, N., Portnyagin, M., Botcharnikov, R., Gurenko, A., Hoernle, K., Holtz, F., 2015. Quantification of the CO₂ budget and H₂O–CO₂ systematics in subduction-zone magmas through the experimental hydration of melt inclusions in olivine at high H₂O pressure. *Earth Planet. Sci. Lett.* 425, 1–11. <https://doi.org/10.1016/j.epsl.2015.05.043>.
- Moore, L.R., Gazel, E., Tuohy, R., Lloyd, A.S., Esposito, R., Steele-MacInnis, M., Hauri, E., Wallace, P.J., Plank, T., Bodnar, R.J., 2015. Bubbles matter: an assessment of the contribution of vapor bubbles to melt inclusion volatile budgets. *Am. Mineral.* 100 (4), 806–823. <https://doi.org/10.2138/am-2015-5036>.
- Moussallam, Y., Médard, E., Georgeais, G., Rose-Koga, E.F., Koga, K.T., Pelletier, B., Bani, P., Shreve, T.L., Grandin, R., Boichu, M., Tari, D., Peters, N., 2021. How to turn off a lava lake? A petrological investigation of the 2018 intra-caldera and submarine eruptions of Ambrym volcano. *Bull. Volcanol.* 83 (5), 36. <https://doi.org/10.1007/s00445-021-01455-2>.
- Moussallam, Y., Rose-Koga, E.F., Koga, K.T., Médard, E., Bani, P., Devidal, J.L., Tari, D., 2019. Fast ascent rate during the 2017–2018 Plinian eruption of Ambae (Aoba) volcano: a petrological investigation. *Contrib. Mineral. Petrol.* 174 (11), 90. <https://doi.org/10.1007/s00410-019-1625-z>.
- Mutch, E.J.F., MacLennan, J., Shorttle, O., Edmonds, M., Rudge, J.F., 2019. Rapid transcrustal magma movement under Iceland. *Nat. Geosci.* 12 (7), 569–574.
- Mutch, E.J.F., MacLennan, J., Shorttle, O., Rudge, J.F., Neave, D.A., 2021. DFENS: diffusion chronometry using finite elements and nested sampling. *Geochem. Geophys. Geosyst.* 22 (4) e2020GC009303.
- Namiki, A., Manga, M., 2006. Influence of decompression rate on the expansion velocity and expansion style of bubbly fluids. *J. Geophys. Res. Solid Earth* 111 (11), 1–17. <https://doi.org/10.1029/2005JB004132>.

- Newcombe, M.E., Plank, T., Barth, A., Asimow, P., Hauri, E., 2020. Water-in-olivine magma ascent chronometry: every crystal is a clock. *J. Volcanol. Geotherm. Res.*, 106872.
- Nicolich, R., Laigle, M., Hirn, A., Cernobori, L., Gallart, J., 2000. Crustal structure of the ionian margin of Sicily: etna volcano in the frame of regional evolution. *Tectonophysics* 329 (1–4), 121–139. [https://doi.org/10.1016/S0040-1951\(00\)00192-X](https://doi.org/10.1016/S0040-1951(00)00192-X).
- Parfitt, E.A., Wilson, L., 1994. Modelling the transition between Hawaiian-style lava fountaining and Strombolian explosive volcanic activity. In: Proceedings of the Abstracts of the 25th Lunar and Planetary Science Conference, 1995, pp. 1049–1050. <http://adsabs.harvard.edu/full/1994LP....25.1049P>.
- Pichavant, M., Di Carlo, I., Rotolo, S.G., Scaillet, B., Burgisser, A., Le Gall, N., Martel, C., 2013. Generation of CO₂-rich melts during basalt magma ascent and degassing. *Contrib. Mineral. Petrol.* 166 (2), 545–561. <https://doi.org/10.1007/s00410-013-0890-5>.
- Portnyagin, M., Hoernle, K., Plechov, P., Mironov, N., Khubunaya, S., 2007. Constraints on mantle melting and composition and nature of slab components in volcanic arcs from volatiles (H₂O, S, Cl, F) and trace elements in melt inclusions from the Kamchatka Arc. *Earth Planet. Sci. Lett.* 255 (1–2), 53–69.
- Portnyagin, M.V., Mironov, N.L., Matveev, S.V., Plechov, P.Y., 2005. Petrology of avachites, high-magnesian basalts of Avachinsky Volcano, Kamchatka: II. Melt inclusions in olivine. *Petrology* 13 (4), 322. *C/C Of Petrologiia*.
- Qin, Z., Lu, F., Anderson, A.T., 1992. Diffusive reequilibration of melt and fluid inclusions. *Am. Mineral.* 77 (5–6), 565–576.
- Rasmussen, D.J., Plank, T.A., Wallace, P.J., Newcombe, M.E., Lowenstern, J.B., 2020. Vapor-bubble growth in olivine-hosted melt inclusions. *Am. Mineral.* 105 (12), 1898–1919.
- Reed, M.H., Munoz-Saez, C., Hajimirza, S., Wu, S.M., Barth, A., Girona, T., Rasht-Behesht, M., White, E.B., Karplus, M.S., Hurwitz, S., 2021. The 2018 reawakening and eruption dynamics of Steamboat Geysir, the world's tallest active geysir. *Proc. Natl. Acad. Sci.* 118 (2).
- Ruprecht, P., Plank, T., 2013. Feeding andesitic eruptions with a high-speed connection from the mantle. *Nature* 500 (7460), 68–72.
- Schiano, P., Clocchiatti, R., Ottolini, L., Busà, T., 2001. Transition of Mount Etna lavas from a mantle-plume to an island-arc magmatic source. *Nature* 412 (6850), 900–904. <https://doi.org/10.1038/35091056>.
- Schiano, P., Eiler, J.M., Hutcheon, I.D., Stolper, E.M., 2000. Primitive CaO-rich, silica-undersaturated melts in island arcs: evidence for the involvement of clinopyroxene-rich lithologies in the petrogenesis of arc magmas. *Geochem. Geophys. Geosyst.* 1 (5) <https://doi.org/10.1029/1999gc000032>.
- Shea, T., Ruth, D., Jollands, M., Ohtaki, K., Ishii, H., Bradley, J., 2023. The presence of silicate melt may enhance rates of cation diffusion in olivine. *Earth Planet. Sci. Lett.* 621, 118370 <https://doi.org/10.1016/j.epsl.2023.118370>.
- Shi, S.C., Towbin, W.H., Plank, T., Barth, A., Rasmussen, D., Moussallam, Y., Lee, H.J. and Menke, W., (2024). PyIRoGlass: An Open-Source, Bayesian MCMC Algorithm for Fitting Baselines to FTIR Spectra of Basaltic-Andesitic Glasses. *Volcanica*.
- Spandler, C., O'Neill, H.S.C., 2010. Diffusion and partition coefficients of minor and trace elements in San Carlos olivine at 1,300 C with some geochemical implications. *Contrib. Mineral. Petrol.* 159, 791–818.
- Steele-MacInnis, M., Esposito, R., Moore, L.R., Hartley, M.E., 2017. Heterogeneously entrapped, vapor-rich melt inclusions record pre-eruptive magmatic volatile contents. *Contrib. Mineral. Petrol.* 172 (4), 1–13. <https://doi.org/10.1007/s00410-017-1343-3>.
- Tonarini, S., Armienti, P., D'Orazio, M., Innocenti, F., 2001. Subduction-like fluids in the genesis of Mt. Etna magmas: evidence from boron isotopes and fluid mobile elements. *Earth Planet. Sci. Lett.* 192 (4), 471–483.
- Tonarini, S., D'Orazio, M., Armienti, P., Innocenti, F., Scribano, V., 1996. Geochemical features of eastern Sicily lithosphere as probed by Hyblean xenoliths and lavas. *Eur. J. Mineral.* 8 (5), 1153–1173.
- Toplis, M.J., 2005. The thermodynamics of iron and magnesium partitioning between olivine and liquid: criteria for assessing and predicting equilibrium in natural and experimental systems. *Contrib. Mineral. Petrol.* 149 (1), 22–39. <https://doi.org/10.1007/s00410-004-0629-4>.
- Trua, T., Esperança, S., Mazzuoli, R., 1998. The evolution of the lithospheric mantle along the N. African Plate: geochemical and isotopic evidence from the tholeiitic and alkaline volcanic rocks of the Hyblean plateau, Italy. *Contrib. Mineral. Petrol.* 131 (4), 307–322. <https://doi.org/10.1007/s004100050395>.
- Turner, S.J., Langmuir, C.H., 2015. The global chemical systematics of arc front stratovolcanoes: evaluating the role of crustal processes. *Earth Planet. Sci. Lett.* 422, 182–193.
- Viccaro, M., Cristofolini, R., 2008. Nature of mantle heterogeneity and its role in the short-term geochemical and volcanological evolution of Mt. Etna (Italy). *Lithos* 105 (3–4), 272–288. <https://doi.org/10.1016/j.lithos.2008.05.001>.
- Wallace, P.J., Plank, T., Bodnar, R.J., Gaetani, G.A., Shea, T., 2021. Olivine-hosted melt inclusions: a microscopic perspective on a complex magmatic world. *Annu. Rev. Earth Planet. Sci.* 49.
- Walter, M.J., 1998. Melting of garnet peridotite and the origin of komatiite and depleted lithosphere. *J. Petrol.* 39 (1), 29–60.
- Zamboni, D., Trella, J., Gazel, E., Sobolev, A.V., Cannatelli, C., Lucchi, F., Batanova, V.G., De Vivo, B., 2017. New insights into the Aeolian Islands and other arc source compositions from high-precision olivine chemistry. *Lithos* 272, 185–191.
- Zuccarello, F., Schiavi, F., Viccaro, M., 2022. The eruption run-up at Mt. Etna volcano: constraining magma decompression rates and their relationships with the final eruptive energy. *Earth Planet. Sci. Lett.* 597, 117821 <https://doi.org/10.1016/j.epsl.2022.117821>.